

Research Article

A Low-Carbon Design Method Integrating Structure Design and Injection Process Design for Injection Molding Machines

Zili Wang , Shuyou Zhang , Lemiao Qiu , Xiaojian Liu , and Heng Li

The State Key Laboratory of Fluid Power and Mechatronic System, Zhejiang University, Hangzhou 310027, China

Correspondence should be addressed to Lemiao Qiu; qiulm@zju.edu.cn

Received 22 March 2019; Accepted 19 August 2019; Published 17 September 2019

Academic Editor: Akhil Garg

Copyright © 2019 Zili Wang et al. This is an open access article distributed under the Creative Commons Attribution License, which permits unrestricted use, distribution, and reproduction in any medium, provided the original work is properly cited.

In the past decades, environmental problems are widely concerned and solved. However, as most solutions, they are methods of “end-of-pipe” treatment which are inefficient and of high cost. Low-carbon design (LCD) is a novel way to solve the problem of pollution emissions at source. Injection molding machine (IMM) as important manufacturing equipment has been widely used in many industries. In the pursuit of high-quality plastic products, the environmental qualities of IMM are often neglected. To achieve low carbon of IMM at source, a LCD method is proposed combining the structure design and injection process design for IMM. At first, LCD decision variables are determined based on interval number theory. Subsequently, the IMM structural carbon emissions and injection molding process carbon emissions are calculated, respectively. Based on this architecture, the carbon emission mathematical model is constructed. To solve the multiobjective optimization problem, the improved strength Pareto evolutionary algorithm based on epsilon dominance (E-SPEA-II) is used, and the design result schemes are sorted using the multiattribute decision-making method for intervals. Finally, the validity of this method is demonstrated by an IMM injection component-integrated low carbon design (ILCD) example.

1. Introduction

Injection molding machine (IMM) is the main equipment for plastic production, which maintains a complex system integrating mechanical, electrical, and hydraulic properties [1]. The production of plastic products is 7.7×10^7 tons in 2016 in China. The annual growth of the plastic-processing industry is 8%. The annual growth rate is in the forefront of the light industry, 1.21% higher than others in the light industry and 2% higher than others in the Chinese national industry [2]. However, as a kind of high-energy consumption equipment, the whole life cycle of an IMM is accompanied by a large number of environmental impacts. The ecological environment properties of plastic products have been considered as Chinese national VOC (volatile organic compounds) emissions and PM 2.5 index. Carbon emission is one of the most important green sustainable development indicators among these ecological environment properties.

A schematic of a typical inline reciprocating screw IMM with hydraulic drive discussed in this paper is shown in

Figure 1. This IMM is a mechatronics equipment which consists of injection molding components (3, 4, 10, 13), feeding components (5), clamping components (1, 2, 14, 15), heating components (12), and hydraulic components (6, 7, 8, 9, 11).

Among the existed LCD researches, scholars focus on two major fields, product structure LCD and product process LCD. Plenty of research studies have been conducted in the study field of product structure LCD [4, 5]. Song and Lee [6] divided the product into several structure parts to analyze the greenhouse gas (GHG) emissions separately. They developed a design system which allowed quick calculation of the GHG emissions of a product that helped product structure low-carbon design. Zhang et al. [7] considered the product as the organic combination of connection units. By analyzing the parts' connection characteristics, they obtained the carbon emissions of each product connection unit. Lu et al. [8] proposed a selection method based on the characteristic of carbon emissions for low-carbon structure design. The total carbon emissions distribution of every product part can be achieved by the

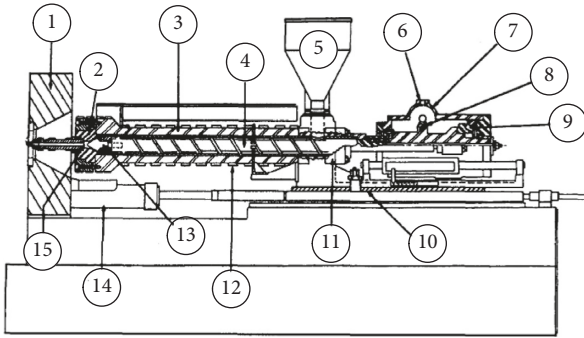


FIGURE 1: Schematic of a typical inline reciprocating screw IMM with hydraulic drive [3]. 1: die head; 2: standard extruder head; 3: extruder barrel; 4: extruder screw; 5: hopper; 6: tachometer drive; 7: hydraulic motor; 8: screw drive system; 9: thrust bearing; 10: air lift for screw removal; 11: hydraulic injection cylinder; 12: heating bands; 13: nonsreturn flow valve assembly; 14: pull-in cylinder; 15: injection chamber.

proposed method. As typical mechatronics equipment, IMM is widely used in many applications. The carbon emissions of the IMM structure grow with increase of the complexity of the IMM structure [9–11]. A number of scholars focus on improving the IMM structure LCD method. Agazzi et al. [12] proposed a new design method to determine the structure of IMM cooling runner in the three-dimensional model. The optimal fluid temperature distribution along cooling is determined. Li et al. [13] used the method of configuration space to optimize the layout design of IMM cooling channel. This method overcomes the limitation of invariable topological structure in the previous design. Both methods mentioned above helped to decrease the carbon emissions of the IMM cooling system.

In the study field of product process LCD, Tan et al. [14] constructed a multiobjective cutting fluid decision-making model considering the quality, cost, and environmental impact for machine tools process planning. It is verified by an example of cutting fluid selection. Sivapirakasam et al. [15] proposed a method hybridizing Taguchi and fuzzy TOPSIS to solve multiresponse parameter optimization problems in green manufacturing. Jiang and Zhang [16] established a machine tool processing selection model for low carbon emissions. A vector projection method is developed in their study to justify machine tool processing alternatives. In addition, injection molding process is a typical reciprocating process. Every step of an injection molding process cycle has been accompanied by carbon emissions [17–19]. Scholars have been studied for years to find the efficient way to reduce the injection molding process carbon emissions. Meekers et al. [20] proposed a method to optimize the injection molding process in order to reduce energy consumption as well as ensuring the part quality. They found that the cooling time had the most sensitive impact on energy consumption. To verify the effect on energy consumption of optimized process parameters, Tranter et al. [21] generated a novel experimental schedule. The result showed that the cooling time incurred the largest variation in energy consumption during the cycle time injection molding process.

LCD problems usually can be considered as the optimization problems. There are two major solutions to the optimization problems. They are evolution algorithm and machine-learning algorithm. Wang et al. [22] proposed a new automatic niching technique based on the affinity propagation clustering and designed a novel niching differential evolution algorithm. It helped to solve the multimodal optimization problems. Liu et al. [23] proposed an adaptive sorting-based environmental selection strategy. An adaptive promising subpopulation sorting-based environmental selection strategy is provided for problems which may have irregular Pareto fronts. Chen et al. [24] proposed an automated neural network search method in optimizing the power output of cleaner energy production systems.

Previous researches have made some achievements in LCD of products. However, the product structure design [25, 26] and the product manufacturing process design [27, 28] are separated in the LCD process. In the structural design of IMMs, there is several uncertainties in the injection process plan because that the injection molding process has not yet been carried out. In the process of injection molding process design, the structure of IMMs has been determined and it could not be modified according to the requirements of low-carbon design. The separation makes the LCD of IMMs lack the overall situation, which affects the accuracy of LCD results. Therefore, an integrated low-carbon design (ILCD) method is proposed combining the structure design and injection process design for IMMs.

This paper proposes a low-carbon design method integrating structure design and injection process design for IMMs. The framework of the new low-carbon design method is introduced in Section 2. Then, a carbon emissions calculation model is proposed in Section 3 in detail. Section 4 presents an optimization method to solve the carbon emissions problem. It helps to find the most proper scheme for IMMs ILCD. Section 5 describes a case study of DSH280/750TW IMM injection component low-carbon design problem. And, the discussion of the results is shown in Section 6. Finally, Section 7 concludes this paper.

2. Framework of the ILCD Method for IMM

The framework of the ILCD method for IMM, which is shown in Figure 2, is illustrated in this section. At first, the decision variables of IMM LCD problem are determined based on the LCD requirement. Considering the uncertainty of ILCD, the related parameters are interval expressed for further dominance comparing. Based on that, the total carbon emissions are divided into structural carbon emissions and injection molding process carbon emissions and, respectively, calculated. In structural carbon emissions calculation part, the raw material carbon emissions are calculated using the Kriging model to fit the unknown structural carbon emissions response; at the meantime, the carbon emissions when manufacturing the IMM are calculated based on the energy consumption model during machine tools manufacturing. On the other side, in injection molding process carbon emissions calculation part, it is divided into four subprocess calculations, of which the

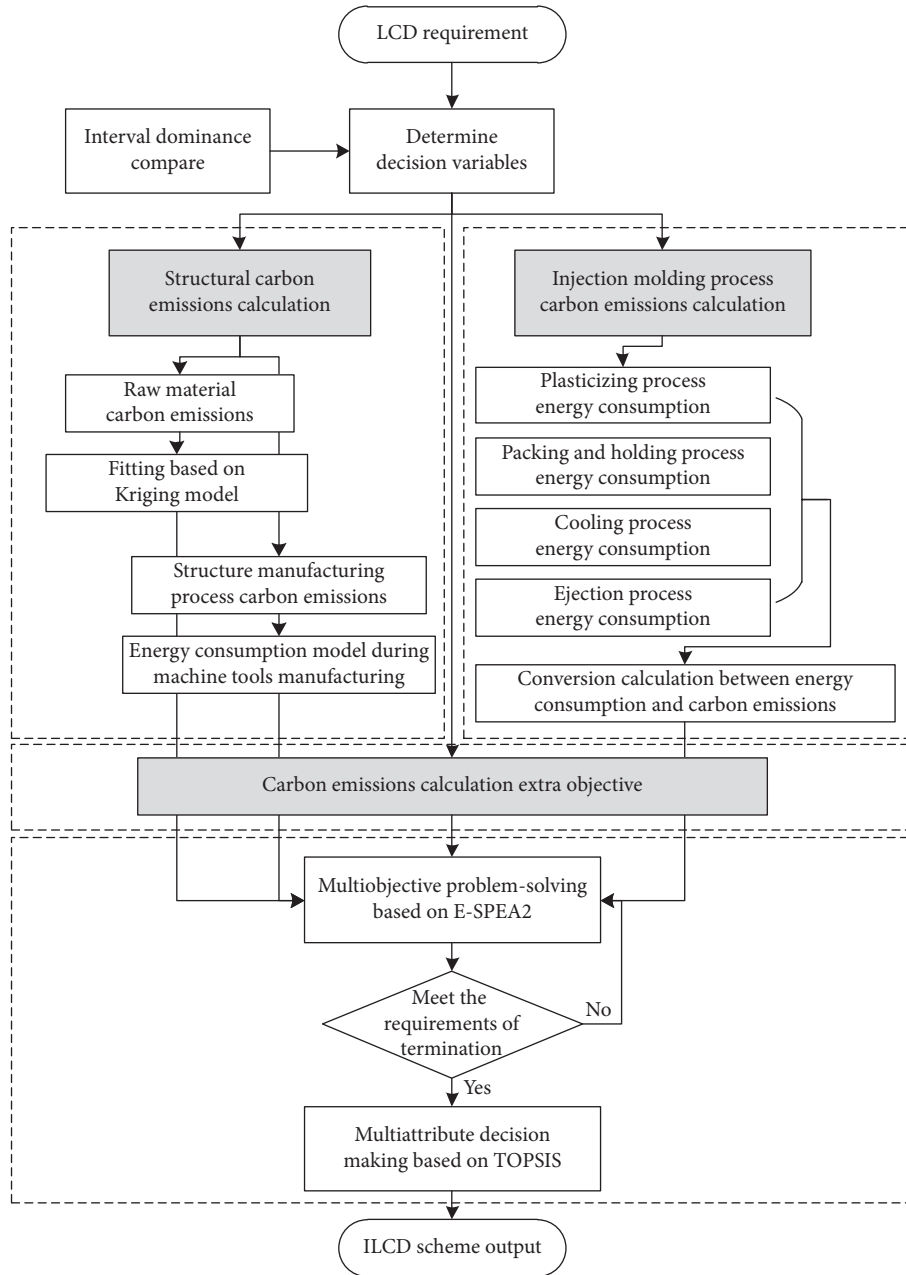


FIGURE 2: Framework of the ILCD method for IMM.

energy consumptions are calculated first. Subsequently, the energy consumptions are converted to carbon emissions. In addition, it will be meaningless if the quality of injection products is not guaranteed in ILCD; thus, the plasticizing capacity is considered as the extra objective in integrated carbon emissions calculation. Above all, the carbon emissions mathematical model can be developed as a three-objective optimization problem, which can be optimized by an improved evolutionary algorithm. Due to the design parameters being interval expressed, the optimal results of Pareto frontier are also the interval numbers. A dynamic multiattribute decision-making method is used to sort the optimal populations. According to the sorting result, ILCD optimal scheme is obtained.

3. ILCD Carbon Emissions Calculation Model

3.1. LCD Decision Variables. In order to develop a carbon emissions calculation model for the integrated LCD, some design parameters should be determined as LCD decision variables. In the IMM life cycle, different LCD decision variables from each stage are stored in set \overline{X}_k , which is shown as follows:

$$\overline{X}_k = \{x_{k_1}, x_{k_2}, x_{k_3}, \dots, x_{k_u}\}, \quad (1)$$

where \overline{X}_k presents the decision variables set at k^{th} stage of the life cycle of IMM and u is the amount of decision variables at k^{th} stage. For example, at the material stage, one

of the decision variables X_{11} is {nonreturn valve (45CrMo) 15 kg, heating bands (stainless steel) 5 kg, and injection ram (HT200) 16.5 kg}. Then, at the manufacturing stage, these raw materials are manufactured with different processes.

In the very beginning of the IMM scheme design stage, the process parameters are uncertain. Therefore, intervals are used to express these uncertain design parameters. The ternary interval A is represented by two numbers, which is expressed as follows:

$$A = [a^-, a^+], \quad (2)$$

where a^- represents the lower limit of A and a^+ represents the upper limit of A .

Definition 1. If $A = [a^-, a^+]$ and $B = [b^-, b^+]$, the distance between A and B can be recorded as $d(A, B)$:

$$d(A, B) = \max\{|a^- - b^-|, |a^+ - b^+|\}. \quad (3)$$

Definition 2. If $A = [a^-, a^+]$ and $B = [b^-, b^+]$, \sqsupset is the maximum interval of A and B , recorded as $[\beta^-, \beta^+]$, where $\beta^- = \max\{a^-, b^-\}$ and $\beta^+ = \max\{a^+, b^+\}$.

As \sqsupset is the maximum interval of A and B , a conclusion can be drawn that $\sqsupset \geq A$ and $\sqsupset \geq B$.

Definition 3 [29, 30]. If $A = [a^-, a^+]$ and $B = [b^-, b^+]$, \sqsupset is the maximum interval of A and B , the relative dominance coefficient of $A \geq B$ can be expressed as follows:

$$RD(A \geq B) = \frac{d(B, \sqsupset)}{d(A, \sqsupset) + d(B, \sqsupset)}. \quad (4)$$

Analogously, the relative dominance coefficient of $A \leq B$ can be expressed as follows:

$$RD(A \leq B) = \frac{d(A, \sqsupset)}{d(A, \sqsupset) + d(B, \sqsupset)}. \quad (5)$$

When two intervals are compared, the one with higher relative dominance is usually chosen by decision makers. According to that, the relative dominance is used to compare the dominant relationship between two intervals. ILCD is conducted as a multiobject problem (MOP):

$$\begin{aligned} \min \quad & f(x, c) = (f_1(x, c_1), f_2(x, c_2), \dots, f_{r_n}(x, c_{r_n})) \\ \text{s.t.} \quad & x \in \overline{X_k} \subseteq R^u, \\ & c_{r_i} = (c_{r_i,1}, c_{r_i,2}, \dots, c_{r_i,r_i})^T, \\ & c_{r_i,r_j} = [c_{r_i,r_j}^-, c_{r_i,r_j}^+], \\ & r_j = 1, 2, \dots, r_l, \end{aligned} \quad (6)$$

where x is the decision variable with u dimensions in decision space $\overline{X_k}$. $f_{r_i}(x, c_{r_i})$ ($1, 2, \dots, r_n$) is the r_i th objective function with interval parameter c_{r_i} and c_{r_j} is the r_j th component of the interval parameter vector c_{r_i} . $f_{r_i}(x, c_{r_i})$ can also be expressed as an interval $[f_{r_i}(x, c_{r_i})^-, f_{r_i}(x, c_{r_i})^+]$.

Definition 4. For $x_{k_1}, x_{k_2} \in \overline{X_k}$, if $\forall k_i \in \{1, 2, \dots, k_u\}$, $\sigma(x_{k_1}, x_{k_2}, k_i) \geq \sigma(x_{k_2}, x_{k_1}, k_i)$ and $\exists k'_i \in \{1, 2, \dots, k_u\}$ that makes $\sigma(x_{k_1}, x_{k_2}, k'_i) > \sigma(x_{k_2}, x_{k_1}, k'_i)$, then x_{k_1} dominates x_{k_2} , expressed as $x_{k_1} >_{\sigma} x_{k_2}$.

Definition 5. For $x_{x^*} \in \overline{X_k}$, if $\nexists x_{k_i} \in \overline{X_k}$ that makes $x_{k_i} >_{\sigma} x_{x^*}$, then x_{x^*} is called the Pareto optimum solution.

3.2. IMM Structural Carbon Emissions Calculation. IMM structural carbon emissions consist of two parts, the carbon emissions of IMM raw material and the carbon emissions of manufacturing an IMM process. Sun [31] proposed a product carbon emissions calculation method which also divides the product carbon emissions into two parts:

$$CM_s = CM_m + CM_p = \sum_{i=1}^{k_1} \sum_{j=1}^{k_2} m_{\text{raw}_{ij}} \gamma_{\text{raw}_i} + \sum_{j=1}^{k_2} \sum_{k=1}^{k_3} t_{jk} \gamma_{\text{proc}_{jk}}, \quad (7)$$

where CM_s represents the IMM structural carbon emissions consumption; the unit is $(\text{co}_2)\text{kg}$. CM_m represents the carbon emissions consumption of the IMM raw material; the unit is $(\text{co}_2)\text{kg}$. CM_p represents the carbon emissions consumption during process manufacturing the IMM; the unit is $(\text{co}_2)\text{kg}$. $m_{\text{raw}_{ij}}$ represents the quantity consumption of the i^{th} kind of material for the j^{th} component; the unit is kg. γ_{raw_i} represents the carbon emissions factor of the i^{th} kind of material; the unit is $(\text{co}_2)\text{kg/kg}$. k_1 represents the amount of material types, while k_2 represents the amount of components. t_{jk} represents the time consumption of the k^{th} process for manufacturing the j^{th} component; the unit is h. $\gamma_{\text{proc}_{jk}}$ represents the carbon emissions factor of the k^{th} process for manufacturing the j^{th} component; the unit is $(\text{co}_2)\text{kg/h}$. k_3 represents the amount of manufacturing processes.

However, at the beginning of IMM LCD, plenty of structural parameters are uncertain. The quantity consumption of IMM is difficult to be calculated. In order to overcome this problem, the Kriging approximate model is used for fitting the carbon emissions consumption of IMM raw material (CM_m). Because of its strong ability to remove noise and high optimization efficiency, the Kriging approximate model is widely used in describing nonlinear problems that are difficult to obtain analytical expressions [32, 33]. Suppose that CM_m can be expressed as follows:

$$CM_m = K(X) = \varphi(X)\omega + \tau(X), \quad (8)$$

where X represents the decision variables set of IMM LCD problem. $\varphi(X)$ represents the estimated carbon emissions consumption of the IMM raw material. ω is the undetermined coefficient of the estimated function. $\tau(X)$ represents a random error function which can be expressed in a variety of forms. In this paper, $\tau(X)$ is expressed as the Gauss distribution in terms of expectation 0 and variance σ^2 . The covariance of the $\tau(X)$ can be expressed as follows:

$$\text{cov}[\tau(x_p), \tau(x_q)] = \sigma^2 R[x_p, x_q], \quad (9)$$

where R represents the correlation matrix. $R(x_p, x_q)$ represents the correlation function of any two samples. $p, q = 1, 2, \dots, n_{\text{ds}}$, where n_{ds} represents the amount of data in the samples. $R(x_p, x_q)$ can be expressed in a variety of forms. For the consistency, $R(x_p, x_q)$ is expressed as Gauss function:

$$R(x_p, x_q) = \exp\left(-\sum_{s=1}^k \theta_s |x_p^s - x_q^s|^2\right), \quad (10)$$

where θ_s represents the s^{th} decision variable and the amount of decision variables is k . According to the Kriging model theory, the estimated response value of the unknown point x can be expressed as follows:

$$\bar{K}(x) = \gamma^T(x) R^{-1}(K - f\bar{\delta}) = \bar{\delta}f(x), \quad (11)$$

where $\bar{\delta}$ represents the estimated value, which can be expressed as follows:

$$\bar{\delta} = (f^T R^{-1} f)^{-1} f^T R^{-1} K, \quad (12)$$

where K represents the column vector of response value of sample data. f represents the unit column vector. $\gamma(x)$ represents the correlation vector between the sample point and the prediction point, which can be expressed as follows:

$$\gamma^T(x) = (R(x, x_{k_1}), R(x, x_{k_2}), \dots, R(x, x_{k_u}))^T. \quad (13)$$

The estimated value of variance can be expressed as follows:

$$\bar{\sigma}^2 = (K - f\bar{\delta})^T R^{-1} \frac{(K - f\bar{\delta})}{s}. \quad (14)$$

θ_s can be obtained by maximum likelihood estimation as

$$\max_{\theta_s > 0} \left(\frac{n_{\text{ds}} \ln(\bar{\sigma}^2) + \ln|R|}{2} \right). \quad (15)$$

Then, initial samples were selected and finite element analysis was used to obtain injection equipment volume. The Latin hypercube sampling method is used to randomly select the sample points in the global design space. In order to ensure the fitting accuracy of the overall output response, the

correlation coefficient is calculated. The closer the correlation coefficient is to 1, the higher the global accuracy of the model is:

$$R_c^2 = 1 - \frac{\sum_{i=1}^{s_R} (K_i - \bar{K}_i)^2}{\sum_{i=1}^{s_R} (K_i - \mu(K))^2}, \quad (16)$$

where K_i represents the output response value of the i^{th} sample point obtained from the finite element analysis software. The amount of sample points is s_R . \bar{K}_i represents the response value obtained from the Kriging model. $\mu(K)$ is the average value of the sample points. In addition, the relative maximum of absolute error is calculated. The closer the relative maximum of absolute error is to 0, the higher the local accuracy of the model is:

$$E_R = \max_{i=1, s_R} \frac{|K_i - \bar{K}_i|}{\sigma(K)}, \quad (17)$$

where $\sigma(K)$ represents the standard deviation of sample points. Only if R_c and E_R meet the requirement of precision, the iterations are complete and the final fitting function is obtained. On the other hand, CM_p is firstly calculated as energy consumption. The components and parts of IMM are manufactured by using computerized numerical control machine tools (CNCMT). The energy consumption model during machine tools manufacturing has already been built [34, 35]. The total energy consumption in manufacturing an IMM is divided into five parts:

$$E_p = E_{\text{PSO}} + E_{\text{PSR}} + E_{\text{PF}} + E_{\text{PTC}} + E_{\text{PC}}, \quad (18)$$

where E_p represents the total energy consumption in manufacturing an IMM. E_{PSO} represents the energy consumption when the CNCMT is standby. E_{PSR} represents the energy consumption during the CNCMT spindle rotation. E_{PF} represents the energy consumption during the CNCMT X-, Y-, and Z-axis feeding. E_{PTC} represents the energy consumption during the CNCMT tool change. E_{PC} represents the energy consumption during the CNCMT A, B, C-axis rotation. The relationship between energy consumption and carbon emissions can be mathematically expressed as

$$CM_p = \sum_{\omega=1}^u E_{\omega} \times F_{\omega} \times H_{\omega}, \quad (19)$$

where E_{ω} represents the consumption of the ω^{th} kind of energy and F_{ω} represents the carbon emissions coefficient of the ω^{th} kind of energy, $\text{kg}(\text{CO}_2)/(\text{kw}\cdot\text{h})$. H_{ω} represents the total time of the ω^{th} kind of energy consumption during single injection molding cycle, h . There are u kinds of energy counted when the carbon emissions of CM_p are calculated.

Above all, the IMM structural carbon emissions can be calculated as follows:

$$\begin{aligned}
CM_S &= CM_m + CM_p = \sum_{i=1}^m f(g_1, g_2, \dots, g_\theta)_i \cdot \rho_i \gamma_{mine_i} + \sum_{j=1}^n t_j \cdot \gamma_{pf_j} \\
&= \varphi(x_{k_1}, x_{k_2}, x_{k_3}, \dots, x_{k_u})\omega + \tau(x_{k_1}, x_{k_2}, x_{k_3}, \dots, x_{k_u}) + \sum_{x_{k_1}, x_{k_2}, x_{k_3}, \dots, x_{k_u}} E_\omega \times F_\omega \times H_\omega.
\end{aligned} \tag{20}$$

3.3. Carbon Emissions Calculation during Injection Molding Process. Injection molding is a repetitive process in which melted polymer (plastic) is injected into mold cavities, where it is held under certain pressure until it is removed into a solid state. Therefore, the whole injection molding process can be regarded as the cycle of multiple same processes, which is shown in Figure 3. It takes a 60-seconds injection molding cycle process as an example.

The carbon emissions during injection molding process are firstly calculated as energy consumption. The heating mode of IMM is the main factor affecting energy consumption in injection molding process. There are several heating modes used in IMM among which the electromagnetic induction heating is the most widely used heating mode. Owing to that, the energy consumption is calculated as it is electromagnetic induction heating IMM. The energy consumption during a whole injection molding process, E_* , which consists of four parts as shown in Figure 4 in grey can be calculated as follows:

$$E_* = E_{plas} + E_{P\&H} + E_{cool} + E_{eiec}, \tag{21}$$

where E_{plas} represents the energy consumption during the plasticizing process, $E_{P\&H}$ represents the energy consumption during the packing and holding process, E_{cool} represents the energy consumption during the cooling process, and E_{eiec} represents the energy consumption during the ejection process. E_{plas} can be calculated as four individual parts as follows:

$$E_{plas} = E_{HB} + E_{HEB} + E_{HS} + E_{HM}, \tag{22}$$

where E_{HB} represents the energy consumption of heating bands, which can be calculated as

$$E_{HB} = \frac{C_W \times k_H \times \Delta T_H \times \pi \times D_S \times L_S}{d_m \times C_C}. \tag{23}$$

E_{HEB} represents the energy consumption of the heating extruder barrel, which can be calculated as

$$E_{HEB} = \frac{m_B \times C_B \times \Delta T_B}{3600 \times t_B}. \tag{24}$$

E_{HS} represents the energy consumption of the heating injection screw, which can be calculated as

$$E_{HS} = \frac{m_s \times C_s \times \Delta T_s}{3600 \times t_s}. \tag{25}$$

E_{HM} represents the energy consumption of the hydraulic motor, which can be calculated as

$$E_{HM} = q_m \times \frac{p}{2\pi}. \tag{26}$$

The schematic of a typical metering-type screw is shown in Figure 4 along with the main screw design parameters.

Based on the experience, the packing pressure is 75% of the injection pressure [36] so that the energy consumption during the packing and holding process, $E_{P\&H}$, can be calculated as follows:

$$E_{P\&H} = 0.75 \times \varphi_V \times V_{inj} \times q_m, \tag{27}$$

where φ_V represents the change ratio in unit volume of the polymer for a given decrease in temperature; the unit is m^3/m^3 . The coefficient of the cooling performance is regarded as the theoretical maximum [37]:

$$E_{cool} = 10^{-3} \times \frac{\rho \times V_{inj} \times [C_C \times \Delta T_H + \omega_f]}{k_c}. \tag{28}$$

It is studied that the energy consumption during ejection process is 25% of the whole process [38] so that the energy consumption during the ejection process, E_{eiec} , can be calculated as follows:

$$E_{eiec} = 0.25 \times (E_{plas} + E_{cool}). \tag{29}$$

Above all, the energy consumption during an injection process cycle can be calculated as

$$\begin{aligned}
E_* &= 1.25 \times \left(\frac{E_T \times k \times \Delta T_H \times \pi \times D_S \times L_S}{d_m \times C_C} + \frac{m_B \times C_B \times \Delta T_B}{3600 \times t_B} \right. \\
&\quad \left. + \frac{m_s \times C_s \times \Delta T_s}{3600 \times t_s} + q_m \times \frac{p}{2\pi} + 10^{-3} \right. \\
&\quad \left. \times \frac{\rho \times V_{inj} \times [C_C \times \Delta T_H + \omega_f]}{k_c} \right) \\
&\quad + 0.75 \times \varphi_V \times V_{inj} \times q_m + 10^{-3} \\
&\quad \times \frac{\rho \times V_{inj} \times [C_C \times \Delta T_H + \omega_f]}{k_c}.
\end{aligned} \tag{30}$$

On this basis, the carbon emissions in a single cycle of injection molding can be calculated as similar as equation (19):

$$CM_* = \sum_{\omega=1}^u E_* \times F_\omega \times H_\omega. \tag{31}$$

Combining equations (30) and (31), the carbon emissions in a single cycle of injection molding can be expressed as

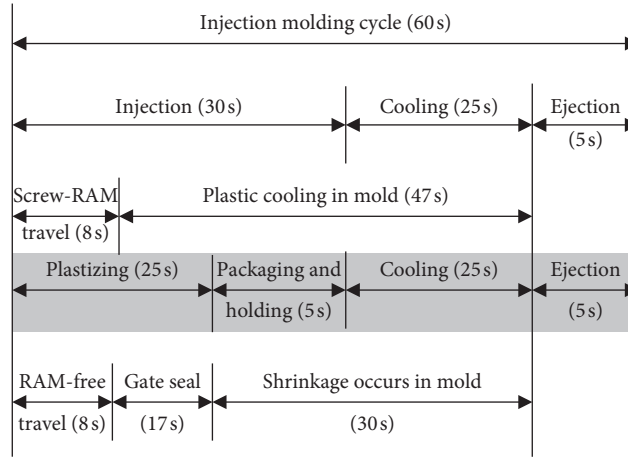
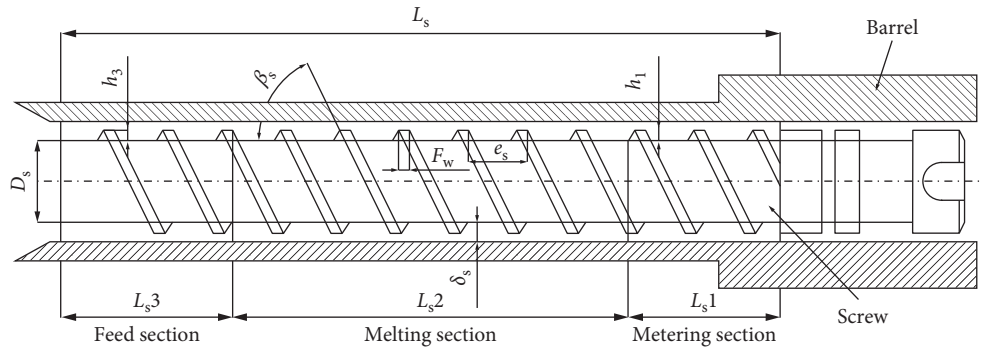


FIGURE 3: Example of the injection molding cycle.


 FIGURE 4: Typical metering-type screw. D_s = screw diameter (normal); β_s = helix angle; e_s = pitch length; F_w = flight width; δ_s = clearance between the screw and the barrel; L_s = screw overall length; L_{s1} = metering section length; L_{s2} = melting section length; L_{s3} = feed section length; h_1 = metering depth; h_3 = feed depth.

$$\begin{aligned}
 CM_* = & \left[1.25 \times \left(\frac{E_T \times k \times \Delta T_H \times \pi \times D_s \times L_s}{d_m \times C_C} \right. \right. \\
 & + \frac{m_B \times C_B \times \Delta T_B}{3600 \times t_B} + \frac{m_s \times C_s \times \Delta T_s}{3600 \times t_s} + q_m \times \frac{p}{2\pi} + 10^{-3} \\
 & \left. \left. \times \frac{\rho \times V_{inj} \times [C_C \times \Delta T_H + \omega_f]}{k_c} \right) + 0.75 \times \varphi_V \times V_{inj} \right. \\
 & \left. \times q_m + 10^{-3} \times \frac{\rho \times V_{inj} \times [C_C \times \Delta T_H + \omega_f]}{k_c} \right] \times F_t \times H_t.
 \end{aligned} \quad (32)$$

3.4. Carbon Emissions Calculation Extra Objective. The basic design purpose of an IMM is to increase the injection molding performance. It will be practically significant to analysis injection molding equipment carbon emission only if the quality of injection products is guaranteed.

Plasticizing capacity is an important index to evaluate the quality of plasticizing products in injection molding equipment. If the plasticizing capability is too low in relation to the shot size required, the chances are that the injected plastic will not be completely melted. Therefore, the conveying capacity of the screw metering section is used to calculate the plasticizing capacity of the screw as the carbon emissions calculation extra objective, which can be express as follows:

$$\begin{aligned}
 q_s = & \frac{\pi^2 D_s^2 h_3 n_s \sin \beta_s \cos \beta_s}{2} - \frac{\pi D_s h_3^3 \sin^2 \beta_s}{12 \mu_1} \frac{\Delta p}{L_{s3}} \\
 & - \frac{\pi^2 D_s^2 \delta^3 \tan \beta_s}{12 \mu_2 e_s} \frac{\Delta p}{L_{s3}}.
 \end{aligned} \quad (33)$$

3.5. Carbon Emissions Mathematical Model. Based on the above mentioned, equation (6) is rewritten as equation (34). In the carbon emissions mathematical model, X_k is taken as the decision variables set; f_1 , f_2 , and f_3 are taken as the

three optimization objectives. It is worth mentioning that q_s as an extra objective is required to obtain the maximum value in ILCD process. However, for the convenience of multiobjective decision at later stage, f_3 is set as $-q_s$.

Besides, in many certain IMM LCD cases, there is an association between those known design parameters. These variables are limited as constraint conditions in the carbon emissions mathematical model:

$$\min_{\bar{x}_k} f(x, c) = (f_1(x, c_1), f_2(x, c_2), f_3(x, c_3))$$

$$f_1(x, c_1) = CM_s = CM_m + CM_p = \varphi(x_{k_1}, x_{k_2}, x_{k_3}, \dots, x_{k_u})\omega + \tau(x_{k_1}, x_{k_2}, x_{k_3}, \dots, x_{k_u}) + \sum_{x_{k_1}, x_{k_2}, x_{k_3}, \dots, x_{k_u}} E_p \times F_\omega \times H_\omega$$

$$f_2(x, c_2) = CM_* = \left[1.25 \times \left(\frac{E_T \times k \times \Delta T_H \times \pi \times D_s \times L_s}{d_m \times C_C} + \frac{m_B \times C_B \times \Delta T_B}{3600 \times t_B} + \frac{m_s \times C_s \times \Delta T_s}{3600 \times t_s} + q_m \right) \times \frac{p}{2\pi} + 10^{-3} \times \frac{\rho \times V_{inj} \times [C_C \times \Delta T_H + \omega_f]}{k_c} \right] + 0.75 \times \varphi_V \times V_{inj} \times q_m + 10^{-3} \\ \times \frac{\rho \times V_{inj} \times [C_C \times \Delta T_H + \omega_f]}{k_c} \times F_t \times H_t$$

$$f_3(x, c_3) = -q_s = -\frac{\pi^2 D_s^2 h_3 n_s \sin \beta \cos \beta}{2} + \frac{\pi D_s h_3^3 \sin^2 \beta}{12\mu_1} \frac{\Delta p}{L_s 3} + \frac{\pi^2 D_s^2 \delta^3 \tan \beta}{12\mu_2 e_s} \frac{\Delta p}{L_s 3}$$

$$\text{s.t. } Z_1, Z_2, \dots, Z_\tau.$$

(34)

4. Optimization Method

4.1. *Optimization Based on E-SPEA-II.* Zitzler et al. [39] proposed the improved strength Pareto evolutionary algorithm (SPEA-II). The advantage of this algorithm is that the less parameter artificially set, the more efficient optimization performance, the higher calculation speed. In addition, this algorithm can obtain the uniform distribution of the Pareto front. However, it still lacks in the maintenance of the target space and convergence speed. In order to overcome these problems, we introduce a novel SPEA-II powered by epsilon dominance which is used by Saxena et al. [40] implemented within the framework of NSGA-II. The improved algorithm flow is shown in Figure 5. The details of the algorithm is as follows:

Step 1. Initialize new population P_0 and an external set E_0 ; set the current generation as $\text{gen} = 0$, the maximum generation as gen_{\max} , the crossover probability as P_c , the mutation probability as P_m ; set N as the number of the evolution population, f^m .

Step 2. Calculate the basic fitness values, $\bar{\nabla}(f^n)$, of individuals in current population P_i and external set E_i as

$$\bar{\nabla}(f^m) = \sum_m \{\Omega(f^m) \mid f^m \in (P_i \cup E_i) \wedge (f^m < f^n)\}, \quad (35)$$

where \wedge represents the conjunctive symbol in mathematical logic, $<$ represents the dominant relationship, and $\Omega(f^m)$ is the pressure value of individual f^m which represents the individual number of f^m as follows:

$$\Omega(f^m) = \alpha(\{n \mid f^n \in (P_i \cup E_i) \wedge (f^n < f^m)\}), \quad (36)$$

where $\alpha(x)$ represents the cardinality function of set x . Considering the influence of the constraint violation $Y(f^n)$ and the intensive rejection between individuals, the final fitness values can be calculated as

$$\nabla(f^n) = \frac{1 - Y(f^n)}{\bar{\nabla}(f^n) + \theta(f^n)}, \quad (37)$$

where $\theta(f^n)$ represents the f^n dispersion index of k -nearest neighbor algorithm [41].

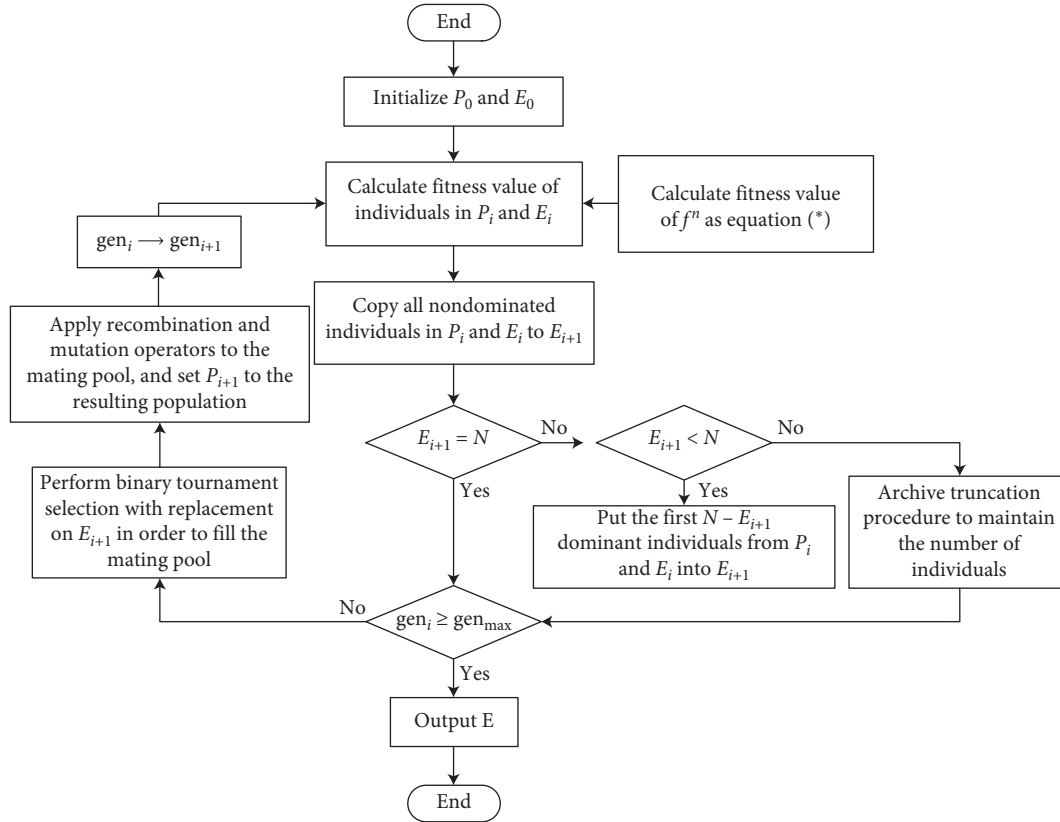


FIGURE 5: Flow chart of E-SPEA-II.

Step 3. Copy the nondominated individuals from current population P_i and external set E_i into next external set E_{i+1} . If the number of individuals in E_{i+1} is larger than N , archive truncation procedure to reduce the individuals number of E_{i+1} , and if the number of individuals in E_{i+1} is less than N , fill E_{i+1} with the current nondominant individuals of E_i and P_i .

Step 4. If $gen_i \geq gen_{max}$, output the individuals in E_{i+1} as Pareto optimal solution; otherwise, go to Step 5.

Step 5. Perform binary tournament selection in E_{i+1} to select the optimal fitness individuals filling into the mate pool.

Step 6. Compare the individuals in E_i and E_{i+1} , select the optimal one into P_i based on dominant relationship. If there is no dominant one between them, randomly choose one to crossover and mutate to generate new individuals in P_{i+1} . Meanwhile, update $gen_i := gen_i + 1$ and go to Step 2.

4.2. Multiattribute Decision Making Method for Intervals.

After optimization by evolution algorithm, the Pareto optimal solution set is obtained. However, there are three s 's in the ILCD problem, the multiattribute decision-making method should be used to weigh the importance of each objective. TOPSIS (technique for order preference by similarity to an ideal solution), proposed by Yoon and Hwang [42], is a widely used method for multiattribute decision.

However, in this paper, the ILCD problem is based on interval numbers and the elements in the decision matrix are intervals. In order to solve the problems, a multiattribute decision-making method for interval numbers is proposed in this paper. After the carbon emissions model has been optimized, several optimization schemes are obtained as shown in matrix D :

$$D = \begin{matrix} W \\ S_1 \\ S_2 \\ S_3 \\ \vdots \\ S_{pn} \end{matrix} \begin{bmatrix} f_1 & f_2 & f_3 \\ [c_{11}^-, c_{11}^+] & [c_{12}^-, c_{12}^+] & [c_{13}^-, c_{13}^+] \\ [c_{21}^-, c_{21}^+] & [c_{22}^-, c_{22}^+] & [c_{23}^-, c_{23}^+] \\ [c_{31}^-, c_{31}^+] & [c_{32}^-, c_{32}^+] & [c_{33}^-, c_{33}^+] \\ \vdots & \vdots & \vdots \\ [c_{pn1}^-, c_{pn1}^+] & [c_{pn2}^-, c_{pn2}^+] & [c_{pn3}^-, c_{pn3}^+] \end{bmatrix}, \quad (38)$$

$$W = (\omega_1, \omega_2, \omega_3).$$

In the decision matrix D , S_1, S_2, \dots, S_{pn} are the final design schemes optimized by the evolution algorithm, where pn is the number of populations. f_1, f_2 , and f_3 are the three optimization objectives. The interval $\tilde{c}_{uv} = [c_{uv}^-, c_{uv}^+]$ ($u = 1, 2, \dots, pn, v = 1, 2, 3$) represents the v^{th} optimization objective of u^{th} scheme. ω_v represents the weight of the v^{th} optimization objective. The specific steps of A are as follows:

Step 1. Normalize the decision matrix D to normalization decision matrix $\tilde{D} = [\tilde{d}_{uv}]_{pn \times 3}$, where

$\tilde{d}_{uv} = [d_{uv}^-, d_{uv}^+]$ represents the interval which is normalized:

$$d_{uv}^- = \frac{c_{uv}^-}{\sqrt{\sum_{u=1}^{pn} (1/2) [(c_{uv}^-)^2 + (c_{uv}^+)^2]}}$$

$$u = 1, 2, \dots, pn, v = 1, 2, 3,$$

$$d_{uv}^+ = \frac{c_{uv}^+}{\sqrt{\sum_{u=1}^{pn} (1/2) [(c_{uv}^-)^2 + (c_{uv}^+)^2]}}$$

$$u = 1, 2, \dots, pn, v = 1, 2, 3.$$
(39)

Step 2. Considering the difference between the importance of the optimization objectives, the normalization decision matrix \tilde{D} is weighted to obtain the weighted normalization decision matrix $\tilde{R} = [\tilde{r}_{uv}]_{pn \times 3}$:

$$\tilde{r}_{uv} = \omega_v \tilde{d}_{uv} = [\omega_v d_{uv}^-, \omega_v d_{uv}^+],$$

$$u = 1, 2, \dots, pn, v = 1, 2, 3,$$
(40)

where ω_v is the weight of the v^{th} optimization objective.

Step 3. Calculate the positive ideal solution A^P and the negative ideal solution A^N as follows:

$$A^P = \{r_1^P, r_2^P, r_3^P\} = \left\{ \left(\max_u \tilde{r}_{uv} \mid v \in U \right), \left(\min_u \tilde{r}_{uv} \mid v \in V \right) \right\},$$
(41)

$$A^N = \{r_1^N, r_2^N, r_3^N\} = \left\{ \left(\min_u \tilde{r}_{uv} \mid v \in U \right), \left(\max_u \tilde{r}_{uv} \mid v \in V \right) \right\},$$
(42)

where U is associated with the benefit criteria, while V is associated with the cost criteria. The maximum and minimum of \tilde{r}_{uv} are calculated based on the relative dominance coefficient RD determined in definition 3. Take r_1^P as an example. RD_{pq} (represents the relative dominance that $\tilde{r}_{p1} \geq \tilde{r}_{q1}$, $p, q = 1, 2, \dots, pn$) is obtained by comparing the elements from $(\tilde{r}_{11}, \tilde{r}_{21}, \dots, \tilde{r}_{pn1})^T$. Hence, the complementary matrix is constructed as $P = (RD_{pq})_{pn \times pn}$, where $RD_{pq} \geq 0$, $RD_{pp} = 1/2$ and $RD_{pq} + RD_{qp} = 1$:

$$RD_p = \sum_{q=1}^{pn} RD_{pq}, \quad p = 1, 2, \dots, pn.$$
(43)

According to the order relationship of RD_p , the maximum and minimum of \tilde{r}_{uv} are obtained.

Step 4. Calculate the distance between every scheme point and the positive ideal solution point (or the negative ideal solution point, respectively):

$$\tilde{g}_u^P = \sqrt{\sum_{v=1}^3 (r_v^{P-} - r_{uv}^-)^2 + \sum_{v=1}^3 (r_v^{P+} - r_{uv}^+)^2},$$
(44)

$$\tilde{g}_u^N = \sqrt{\sum_{v=1}^3 (r_v^{N-} - r_{uv}^-)^2 + \sum_{v=1}^3 (r_v^{N+} - r_{uv}^+)^2}.$$
(45)

Step 5. Calculate the relative closeness RC_u .

$$RC_u = \frac{\tilde{g}_u^-}{\tilde{g}_u^+ + \tilde{g}_u^-}, \quad u = 1, 2, \dots, pn.$$
(46)

Step 6. The ILCD schemes are sorted based on the relative closeness RC_u . In the ILCD carbon emissions optimization problem, the solution is to minimize all three objectives. So the smaller the relative closeness RC_u is, the better the ILCD scheme is.

5. A Case Study: Structure Optimization Design of the IMM Injection Component

In this section, a case study is conducted in an IMM injection component LCD process, which is provided by Zhejiang Sound Machine Manufacturing Co. Ltd. The model of the IMM is DSH280/750TW. The main design parameters of DSH280/750TW IMM injection component is presented in Table 1 as design requirement. The details of the 3D model are shown in Figure 6. According to design experiment and design requirement, eight parameters are chosen as ILCD decision variables. The ILCD decision variables are shown in Table 2 which consists of four structure design parameters and four injection process parameters.

After the ILCD requirement and decision variables are determined, the ILCD carbon emissions calculation model can be constructed. The Kriging model is used in DSH280/750TW injection component carbon emissions calculation. There are four structure design parameters chosen in Table 2 as decision variables which are L_{HB} , h_3 , β , e . Twenty-six initial sample points are obtained based on design cases to fit the volume of the barrel and screw which is sampled in 3D modeling software. The Kriging model iterative process data of injection component carbon emissions are shown in Table 3. According to equations (8)–(17), the volume of the barrel and screw of IMM can be expressed as

$$V_{b\&s} = 5.823 \times 10^{-2} h_3^4 + 4.524 \times 10^{-4} L_{HB} \beta_S h_3 \delta_S + 1.587$$

$$\times 10^{-5} L_{HB} \beta_S^2 \delta_S + 3.241 \times 10^{-5} L_{HB} \beta_S^2 h_3 + 6.421$$

$$\times 10^{-3} \beta_S h_3^2 \delta_S - 12.531.$$
(47)

The raw material of the barrel and screw of DSH280/750TW IMM is HT300 carbon steel. The density of HT300 carbon steel is 7300 kg/m^3 , and according to IPCC, the carbon emission of HT300 carbon steel per kilogram is 1.06 kg. So the carbon emissions consumption of IMM raw material can be expressed as

TABLE 1: Main design parameters of DSH280/750TW injection component.

Parameter	D_s	r_{ld}	V_C	m_{inj}	v_{inj}	q_s	P_{inj}	n_s	N_I	N_T	N_a
Value	50	25:1	471	428	365	48	159	350	45	Open nozzle	5
Unit	mm		cm ³	g	g/s	cm ³ /s	MPa	r/min	mm		

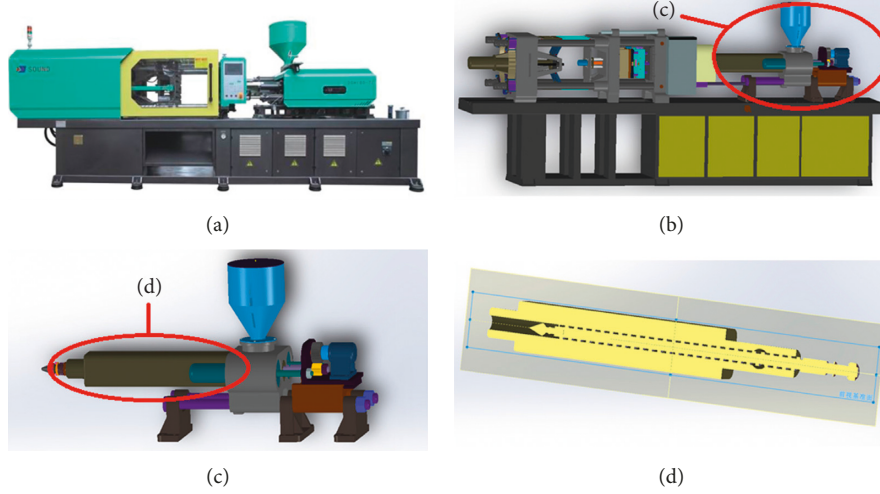


FIGURE 6: DSH280/750TW IMM 3D model. (a) IMM physical view. (b) IMM 3D model. (c) IMM injection component 3D model. (d) Cross section of the screw and barrel.

TABLE 2: ILCD decision variables of DSH280/750TW injection component.

Parameter	L_{HB}	h_3	β_s	δ_s	ΔT_B	ΔT_s	t_B	t_s
Unit	mm	mm	°	mm	K	K	s	s

TABLE 3: Kriging model iterative process data of injection component carbon emissions.

Number of iterations	Number of samples	R_c^2 (%)	E_R (%)
0	26	0.6152	0.4263
1	41	0.7432	0.3412
2	53	0.8014	0.2581
3	60	0.8503	0.1387
4	65	0.8821	0.0945
5	68	0.9142	0.0695
6	69	0.9309	0.0652
7	70	0.9352	0.0623

$$\begin{aligned}
CM_m = & (5.823 \times 10^{-2} h_3^4 + 4.524 \times 10^{-4} L_{HB} \beta_s h_3 \delta_s + 1.587 \\
& \times 10^{-5} L_{HB} \beta_s^2 \delta_s + 3.241 \times 10^{-5} L_{HB} \beta_s^2 h_3 + 6.421 \\
& \times 10^{-3} \beta_s h_3^2 \delta_s - 12.531) \times 7.3 \times 10^{-3} \times 1.06.
\end{aligned} \quad (48)$$

On the other hand, CM_p are firstly calculated as energy consumption. The injection screw 2D process sketch of DSH280/750TW is shown in Figure 7 which contains

geometric parameter information and surface roughness information. And the machining process card of DSH280/750TW injection screw is shown in Table 4. As in this ILCD case, the decision variables have been already determined and the related process steps are extracted in Table 5, so that the energy consumption is calculated in each related process step. According to equation (19), the carbon emissions of manufacturing the DSH280/750TW injection component can be expressed as (the current situation of electric power structure in China of 2017 is shown in Table 6 along with the corresponding carbon emission coefficient):

$$\begin{aligned}
CM_p = & \left(1000 \times (500 + 500 \times 0.5) \times \tau_{HB1} L_{HB} + 1500 \right. \\
& \times (1000 + 1000 \times 0.1) \times \tau_{HB2} L_{HB} + 350(300 + 240 \\
& \times 0.1) \sqrt{(\tau_{h1} h_3)^2 + (\tau_{\beta1} \beta_s)^2} + 500(340 + 280 \\
& \times 0.02) \sqrt{(\tau_{h2} h_3)^2 + (\tau_{\beta2} \beta_s)^2} \left. \right) \\
& \times (68.4\% \times 5.136 + 19.6\% \times 1.347 + 5.3\% \\
& \times 0.054 + 4\% \times 0.987 + 1.7\% \times 1.121).
\end{aligned} \quad (49)$$

After that, the IMM injection component carbon emissions and the carbon emissions during injection plasticizing process can be calculated, respectively. Finally, the integrated carbon emissions mathematical model with extra objective is built and equation (34) is rewritten as follows:

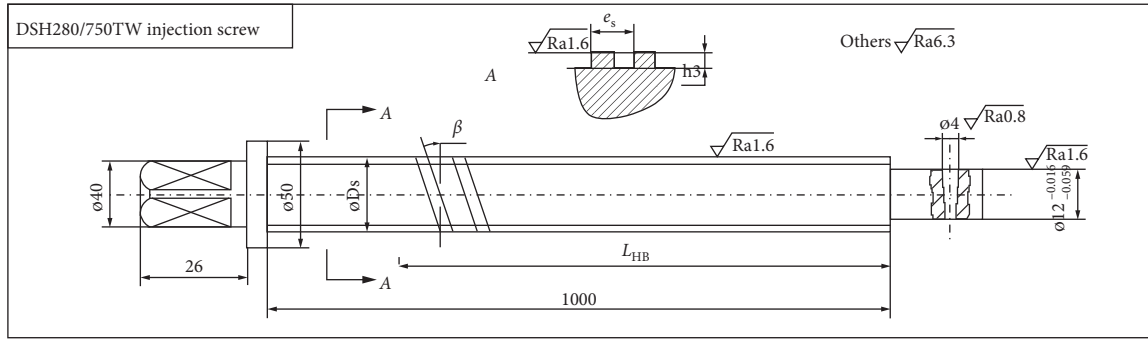


FIGURE 7: DSH280/750TW injection screw 2D process sketch.

TABLE 4: Machining process card of DSH280/750TW injection screw.

Machining process card			Product model	DSH280/750TW
Material	38CrMoAlA	Rough type	Component name	Injection screw
No.	Work procedure names	Process contents	Equipment	Dimension of rough Clamping
10	Lathe	Rough turning the cylinder of D_s	C620-1 horizontal lathe	3-jaw chuck
20	Lathe	Finish turning the cylinder of D_s	C620-1 horizontal lathe	3-jaw chuck
30	Modulation	Modulating to HB240-270		
40	Lathe	Rough turning the cylinder of $\varnothing 50$	C620-1 horizontal lathe	3-jaw chuck
50	Lathe	Finish turning the cylinder of $\varnothing 50$	C620-1 horizontal lathe	3-jaw chuck
60	Lathe	Finish turning the cylinder of $\varnothing 50$	C620-1 horizontal lathe	3-jaw chuck
70	Lathe	Finish turning the cylinder of $\varnothing 50$	C620-1 horizontal lathe	3-jaw chuck
80	Milling	Rough milling the cylinder of D_s	X53T vertical milling machine	Tonger
90	Milling	Finish milling the cylinder of D_s	X53T vertical milling machine	Tonger
100	Check			

TABLE 5: Energy consumption of each related process step.

Operation	Feature contents	Processing parameters	Machine tool	Energy consumption
Turning (No. 10, No. 11)	Rough turning the cylinder of D_s	$n_t = 500, f_t = 0.5, v_z = 500,$ $\overline{F}_Z = 1000$	C620-1 horizontal lathe	$\overline{F}_Z (v_z + n_t f_t) \tau_{HB1} L_{HB}$ [43]
	Finish turning the cylinder of D_s	$n_t = 1000, f_t = 0.1, v_z = 1000,$ $\overline{F}_Z = 1500$	C620-1 horizontal lathe	$\overline{F}_Z (v_z + n_t f_t) \tau_{HB2} L_{HB}$ [43]
Milling (No. 80, No. 90)	Rough milling the cylinder of D_s	$n_t = 240, f_m = 0.1, v_z = 300,$ $\overline{F}_Z = 350$	X53T vertical milling machine	$\overline{F}_Z (v_z + n_t f_t) \sqrt{(\tau_{h1} h_3)^2 + (\tau_{\beta 1} \beta_s)^2}$ [43]
	Finish milling the cylinder of D_s	$n_t = 280, f_t = 0.02, v_z = 340,$ $\overline{F}_Z = 500$	X53T vertical milling machine	$\overline{F}_Z (v_z + n_t f_t) \sqrt{(\tau_{h2} h_3)^2 + (\tau_{\beta 2} \beta_s)^2}$ [43]

TABLE 6: Current situation of electric power structure in China [44].

Types of power	Thermal power	Hydroelectric power	Wind power	Nuclear power	Photovoltaic power
Proportion (%)	68.4	19.6	5.3	4.0	1.7
Carbon emission coefficient	5.136 kg (co ₂)/(kw·h)	1.347 kg (co ₂)/(kw·h)	0.054 kg (co ₂)/(kw·h)	0.987 kg (co ₂)/(kw·h)	1.121 kg (co ₂)/(kw·h)

$$\left\{ \begin{array}{l} \text{find } x = \{L_{\text{HB}}, \beta_s, h_3, \delta_s, \Delta T_B, \Delta T_s, t_B, t_s\} \\ \min_x f_1 \\ \min_x f_2 \\ \max_x f_3 \\ \text{s.t. } d_B = D_s + 2\delta_s, \end{array} \right.$$

$$\begin{aligned} f_1(x, s_1) = \text{CM}_s = \text{CM}_m + \text{CM}_p = & \left(5.823 \times 10^{-2} h_3^4 + 4.524 \times 10^{-4} L_{\text{HB}} \beta_s h_3 \delta_s + 1.587 \times 10^{-5} L_{\text{HB}} \beta_s^2 \delta_s \right. \\ & \left. + 3.241 \times 10^{-5} L_{\text{HB}} \beta_s^2 h_3 + 6.421 \times 10^{-3} \beta_s h_3^2 \delta_s - 12.531 \right) \\ & \times 7.3 \times 10^{-3} \times 1.06 + 7.5 \times 10^5 \times \tau_{\text{HB1}} L_{\text{HB}} + 1.65 \times 10^6 \times \tau_{\text{HB2}} L_{\text{HB}} + 1.134 \times 10^5 \sqrt{(\tau_{h2} h_3)^2 + (\tau_{\beta 2} \beta_s)^2} \\ & + 1.728 \times 10^5 \sqrt{(\tau_{h2} h_3)^2 + (\tau_{\beta 2} \beta_s)^2} \times 4.96, \end{aligned}$$

$$\begin{aligned} f_2(x, s_2) = \text{CM}_* = E_{\text{plas}} \times F_{\text{plas}} \times H_{\text{plas}} \\ = \left(\frac{C_W \times k_m \times \Delta T_H \times \pi \times d_B \times L_{\text{HB}}}{10^6 \times d_m \times C_C} + \frac{m_B \times C_B \times \Delta T_B}{t_B} + \frac{m_s \times C_s \times \Delta T_s}{t_s} + q_m \frac{p_Z}{2\pi} \cdot n_s \cdot \frac{10^3 \times \mu_{\text{mt}}}{9550} \right) \times 5.136 \times \frac{120}{3600}, \end{aligned}$$

$$f_3(x, c_3) = -q_s = -\frac{\pi^2 D_s^2 h_3 n_s \sin \beta_s \cos \beta_s}{2} + \frac{\pi D_s h_3^3 \sin^2 \beta_s}{12\mu_1} \frac{\Delta p}{L_s 3} + \frac{\pi^2 D_s^2 \delta_s^3 \tan \beta_s}{12\mu_2 e_s} \frac{\Delta p}{L_s 3}.$$

(50)

The main design parameters of DSH280/750TW IMM are shown in Table 7, in which the decision variables are in grey. Some of the design parameters are unknown, so they are expressed as interval numbers.

The initial range of the decision variables in ILCD problem is limited according to the design experiment as follows: L_{HB} 500–100 mm, h_3 2.4–5.7 mm, β_s 25–30°, δ_s 10–25 mm, ΔT_B 5–60 K, ΔT_s 150–250 K, t_B 60–120 s, and t_s 60–120 s. Equation (50) is optimized based on the method in Section 4. In order to reduce the unnecessary complexity of algorithm, the initial population is set at 50. The crossover probability is 0.9, and the mutation probability is 0.1, the distribution indexes of which are all 20. In this three-objective optimization problem, the generation is set at 100. The Pareto front of the ILCD results after 100 generations is

shown in Figure 8. It is worth noting that the Pareto front is also an interval front. In Figure 8, the red points represent the upper limit of the optimized results and the blue points represent the lower limit of the optimized results. The detailed results after 100 generations are shown in Table 8. The number in Table 8 represents the serial number of the population. This means there are fifty optimized ILCD schemes that should be compared using the multiattribute decision-making method mentioned in Section 4.2.

The results in Table 8 are firstly normalized and weighted according to the importance of each optimization objective. In this case, the weight vector is set as $W = (\omega_1, \omega_2, \omega_3) = (0.4, 0.4, 0.2)$. Based on that, the positive ideal solution and the negative ideal solution are calculated:

$$\begin{aligned} A^P &= \{(0.059966, 0.104939), (0.064556, 0.060065), (0.031284, 0.030488)\}, \\ A^N &= \{(0.053186, 0.090145), (0.048758, 0.050440), (0.024854, 0.025065)\}. \end{aligned} \quad (51)$$

According to (44)–(46), the relative closeness RC_u of each ILCD scheme is calculated. The detailed results of $\bar{g}_u^P, \bar{g}_u^N, \text{RC}_u$ are shown in Table 9. The fifty Pareto optimal schemes are arranged from small to large according to RC_u .

In this case, the solution is to minimize all three objectives. So the smaller the relative closeness RC_u is, the better the ILCD scheme is. In Table 10, the best ten schemes are shown with decision variables.

TABLE 7: Main design parameters of DSH280/750TW.

Parameter	Interval value	Unit
d_B	70–100	mm
L_{HB}	—	mm
m_B	10–50	kg
C_B	0.46	kJ/(kg·K)
q_m	1–5	L/r
μ_{mt}	0.5–0.9	
m_S	10–50	kg
C_S	0.46	kJ/(kg·K)
n_S	350	r/min
D_S	50	mm
h_3	—	mm
β_S	—	°
δ_S	—	mm
e_s	2.5–3.5	mm
L_S^3	200–500	mm
C_W	0.25–0.80	kJ/(kg·K)
C_C	0.9	kJ/(kg·K)
k_m	0.16	w/(m·k)
ΔT_H	50–160	K
ΔT_B	—	K
ΔT_S	—	K
d_m	0.1–2.5	mm
t_B	—	s
t_S	—	s
p_Z	0.5–20	MPa
μ_1	1000–5000	Pa·s
μ_2	1000–5000	Pa·s
Δp	20–120	MPa

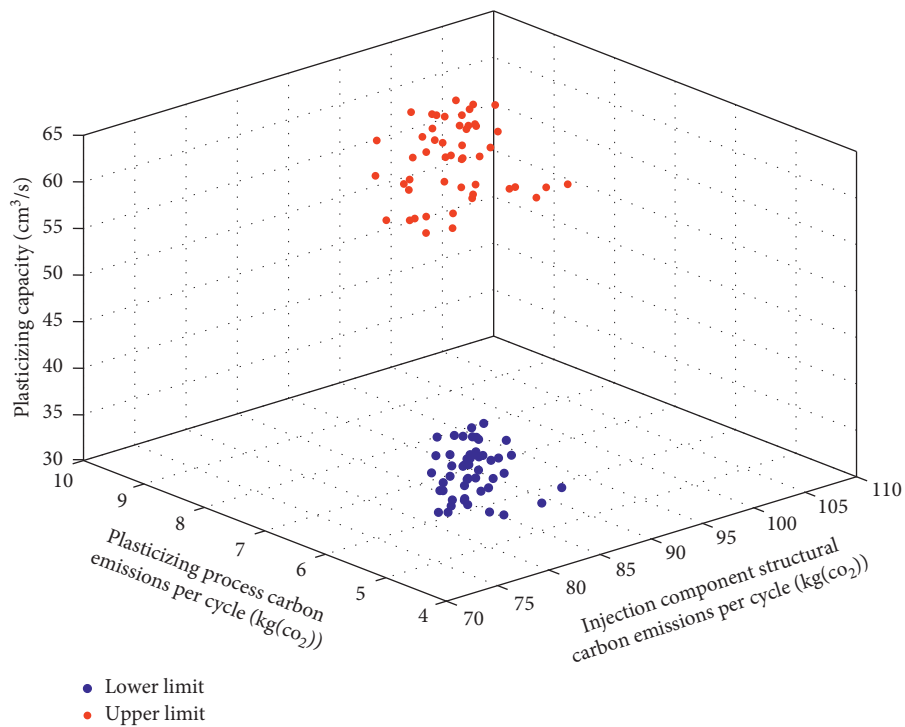


FIGURE 8: Pareto optimal front.

TABLE 8: Detailed results after 100 generations.

No.	CM _S (kg (co ₂))	CM _p (kg (co ₂))	q _S (cm ³ /s)
1	<79.85, 102.89>	<4.72, 9.15>	<34.17, 49.36>
2	<80.07, 102.28>	<5.09, 9.03>	<43.01, 59.96>
3	<77.24, 94.35>	<5.28, 9.28>	<37.10, 58.11>
4	<77.12, 98.17>	<4.51, 8.53>	<38.53, 53.68>
5	<78.56, 99.38>	<4.88, 8.54>	<36.75, 52.49>
6	<75.24, 94.50>	<5.02, 8.76>	<35.23, 50.78>
7	<81.25, 103.96>	<4.33, 8.27>	<35.96, 51.29>
8	<75.57, 94.81>	<5.19, 8.91>	<38.94, 54.21>
9	<82.96, 105.19>	<4.29, 7.96>	<37.15, 53.10>
10	<78.13, 100.67>	<5.08, 8.93>	<39.21, 54.98>
11	<74.85, 102.50>	<4.47, 7.86>	<37.58, 53.92>
12	<82.37, 101.14>	<5.68, 9.02>	<40.28, 55.97>
13	<78.52, 98.57>	<5.17, 8.59>	<38.71, 56.42>
14	<76.39, 94.96>	<4.37, 8.13>	<36.52, 51.37>
15	<80.57, 100.02>	<4.93, 8.54>	<39.52, 56.36>
16	<73.58, 90.36>	<4.58, 8.06>	<36.90, 58.32>
17	<75.48, 99.42>	<4.63, 8.26>	<39.01, 58.23>
18	<78.32, 96.89>	<5.35, 9.18>	<37.25, 52.19>
19	<79.62, 97.82>	<5.26, 9.05>	<38.29, 56.28>
20	<80.34, 98.89>	<5.15, 8.96>	<39.32, 57.15>
21	<79.25, 98.17>	<5.08, 9.36>	<40.25, 59.68>
22	<80.16, 99.78>	<5.19, 9.28>	<41.01, 57.58>
23	<77.45, 97.82>	<4.92, 8.75>	<38.29, 53.85>
24	<78.62, 96.85>	<5.07, 8.07>	<40.18, 55.58>
25	<76.18, 94.28>	<4.75, 9.11>	<36.89, 49.98>
26	<77.13, 93.26>	<5.12, 8.28>	<39.35, 51.04>
27	<75.18, 98.25>	<4.78, 8.68>	<37.19, 50.47>
28	<74.38, 96.27>	<4.85, 9.01>	<38.29, 56.31>
29	<78.34, 93.28>	<4.93, 9.12>	<38.12, 55.07>
30	<80.93, 100.98>	<5.08, 8.21>	<36.82, 53.39>
31	<74.36, 93.28>	<4.66, 8.47>	<37.12, 52.11>
32	<79.15, 101.25>	<5.42, 8.16>	<41.19, 53.61>
33	<78.96, 100.41>	<5.06, 9.08>	<40.12, 54.98>
34	<80.13, 103.98>	<5.18, 8.91>	<39.16, 56.78>
35	<75.16, 102.15>	<4.93, 9.12>	<37.82, 57.12>
36	<77.79, 99.58>	<4.98, 9.03>	<40.23, 55.19>
37	<78.91, 102.25>	<5.08, 9.31>	<41.98, 59.71>
38	<76.82, 100.98>	<5.33, 9.28>	<40.02, 58.46>
39	<81.24, 104.78>	<4.83, 9.09>	<39.85, 58.92>
40	<80.03, 102.64>	<4.71, 9.17>	<42.16, 57.21>
41	<79.13, 101.18>	<5.19, 9.03>	<37.16, 59.18>
42	<79.82, 103.87>	<5.27, 9.27>	<38.89, 56.71>
43	<77.46, 100.13>	<4.99, 8.89>	<42.75, 58.76>
44	<81.06, 101.98>	<4.92, 8.93>	<37.74, 57.99>
45	<75.21, 93.51>	<4.58, 8.32>	<37.83, 52.62>
46	<79.83, 98.56>	<5.17, 9.08>	<41.39, 60.04>
47	<79.01, 97.15>	<4.79, 9.00>	<40.15, 58.27>
48	<77.96, 98.18>	<5.29, 8.97>	<39.85, 57.65>
49	<76.82, 99.47>	<5.31, 9.16>	<42.07, 59.42>
50	<78.91, 102.46>	<4.98, 9.12>	<38.65, 59.16>

TABLE 9: Detailed results of \bar{g}_u^P, \bar{g}_u^N , and RC_u .

No.	\bar{g}_u^P	\bar{g}_u^N	RC_u
1	0.0142	0.0164	0.5359
2	0.0079	0.0193	0.7099
3	0.0132	0.0160	0.5482
4	0.0171	0.0103	0.3765
5	0.0138	0.0128	0.4819
6	0.0164	0.0110	0.4018
7	0.0183	0.0150	0.4508
8	0.0139	0.0138	0.4982
9	0.0190	0.0165	0.4654
10	0.0100	0.0163	0.6189
11	0.0187	0.0128	0.4063
12	0.0054	0.0222	0.8034
13	0.0112	0.0150	0.5732
14	0.0213	0.0057	0.2126
15	0.0118	0.0148	0.5553
16	0.0226	0.0061	0.2123
17	0.0162	0.0117	0.4195
18	0.0113	0.0167	0.5952
19	0.0101	0.0166	0.6217
20	0.0098	0.0165	0.6279
21	0.0103	0.0173	0.6254
22	0.0083	0.0185	0.6909
23	0.0135	0.0127	0.4852
24	0.0143	0.0128	0.4726
25	0.0174	0.0107	0.3808
26	0.0166	0.0112	0.4034
27	0.0156	0.0113	0.4188
28	0.0151	0.0123	0.4496
29	0.0157	0.0125	0.4425
30	0.0123	0.0153	0.5534
31	0.0195	0.0070	0.2626
32	0.0102	0.0183	0.6423
33	0.0097	0.0167	0.6321
34	0.0075	0.0195	0.7216
35	0.0115	0.0167	0.5927
36	0.0111	0.0155	0.5825
37	0.0080	0.0196	0.7091
38	0.0077	0.0195	0.7177
39	0.0102	0.0194	0.6564
40	0.0117	0.0177	0.6031
41	0.0088	0.0180	0.6713
42	0.0064	0.0208	0.7653
43	0.0106	0.0165	0.6086
44	0.0105	0.0170	0.6179
45	0.0199	0.0064	0.2426
46	0.0093	0.0175	0.6520
47	0.0136	0.0137	0.5008
48	0.0097	0.0169	0.6347
49	0.0085	0.0187	0.6881
50	0.0096	0.0180	0.6521

6. Discussion

Based on the results obtained above, the discussion of the effectiveness of the ILCD method is presented by comparing the algorithm used in this paper to two classic multiobjective optimization algorithms (NSGA-II [45] and IP-MOEA [46]). To compare the performance of the three algorithms

in a fair way, the same parameters are set in all three algorithms: The initial population is set at 50. The crossover probability is 0.9, and the mutation probability is 0.1. In order to measure the algorithmic performance, the hypervolume index, the distribution degree, and the imprecision index [46] are calculated. The hypervolume index is calculated as

TABLE 10: Best ten ILCD schemes.

Unit	L_{HB} mm	h_3 mm	β_s °	δ_s mm	ΔT_B K	ΔT_s K	t_B s	t_s s	CM _S kg (co ₂)	CM _P kg (co ₂)	q_s cm ³ /s	
Scheme no.	16	790.2	4.89	29.5	17.4	23.1	182.3	103.2	104.8	<73.58, 90.36>	<4.58, 8.06>	<36.90, 58.32>
	14	781.3	4.91	28.9	16.9	24.5	183.6	104.1	104.3	<76.39, 94.96>	<4.37, 8.13>	<36.52, 51.37>
	45	782.9	4.96	29.1	17.3	24.1	184.2	104.5	105.1	<75.21, 93.51>	<4.58, 8.32>	<37.83, 52.62>
	31	791.2	4.90	29.2	17.1	24.0	183.9	103.7	105.9	<74.36, 93.28>	<4.66, 8.47>	<37.12, 52.11>
	4	792.9	5.00	27.2	15.2	24.9	185.2	104.2	106.2	<77.12, 98.17>	<4.51, 8.53>	<38.53, 53.68>
	25	786.1	4.91	28.5	18.6	25.6	186.1	104.9	107.9	<76.18, 94.28>	<4.75, 9.11>	<36.89, 49.98>
	6	787.3	4.92	28.1	17.9	25.1	185.6	105.2	107.1	<75.24, 94.50>	<5.02, 8.76>	<35.23, 50.78>
	26	790.4	4.96	28.3	18.1	25.6	185.3	105.6	106.5	<77.13, 93.26>	<5.12, 8.28>	<39.35, 51.04>
	11	793.1	4.90	27.9	17.7	25.9	186.0	105.3	106.4	<74.85, 102.50>	<4.47, 7.86>	<37.58, 53.92>
	27	789.6	4.84	27.8	18.2	26.1	186.2	105.9	108.1	<75.18, 98.25>	<4.78, 8.68>	<37.19, 50.47>

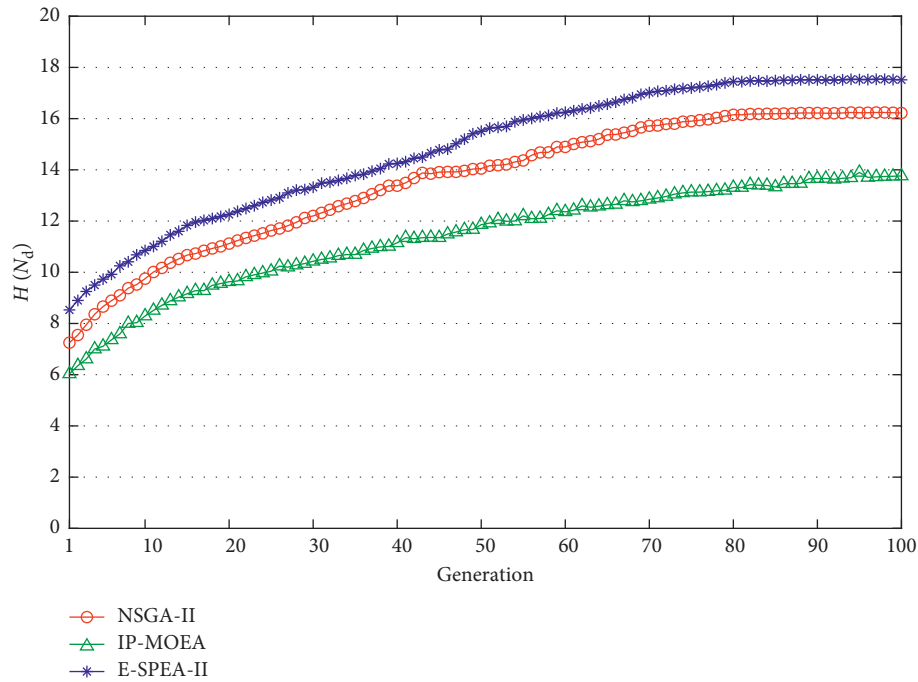


FIGURE 9: Hypervolume (median).

TABLE 11: Distribution degree of three algorithms.

	E-SPEA-II	NSGA-II	IP-MOEA
$D(X)$	0.0834	0.1072	0.2912
Proportion (%)	100	77.80	28.64

$$H(N_d) := \wedge \left(\bigcup_{f(x) \in N_d} \{x \mid f(x_{ref}) \succ y \succ f(x)\} \right), \quad (52)$$

where N_d is a standard nondominated set, x_{ref} represents the reference point, $\wedge(\cdot)$ is the Lebesgue measurement, and \succ represents the Pareto dominant relationship. The hypervolume index can not only reflect the degree of approximation of the Pareto front and the real Pareto front but also characterize the distribution of the Pareto front. The larger the hypervolume index is, the closer the front of the method is to the Pareto front and also the better the distribution of

the front points. However, the distribution of the front points cannot be ideally quantified by the hypervolume index, so the distribution degree is calculated to measure the distribution of the algorithm precisely:

$$D(X) = - \sqrt{\frac{\sum_{j=1}^N (d^*(X) - d(x_j))^2}{(N-1)}}, \quad (53)$$

where $x_j \in X$ and $d(x_j) = \min \sum_{i=1}^m |f_i(x_j) - f_i(x_i)|$, $j = 1, 2, \dots, N$ represents the crowding distance of x_j in target space. $d^*(X) = 1/N (\sum_{j=1}^N d(x_j))$ is the average crowding distance of X . The smaller the distribution degree is, the more uniform the distribution of the optimization front is. The imprecision index is calculated as a quantity of the amount of uncertainty in the algorithm population. This might be measured as the added volume of all solutions in the front:

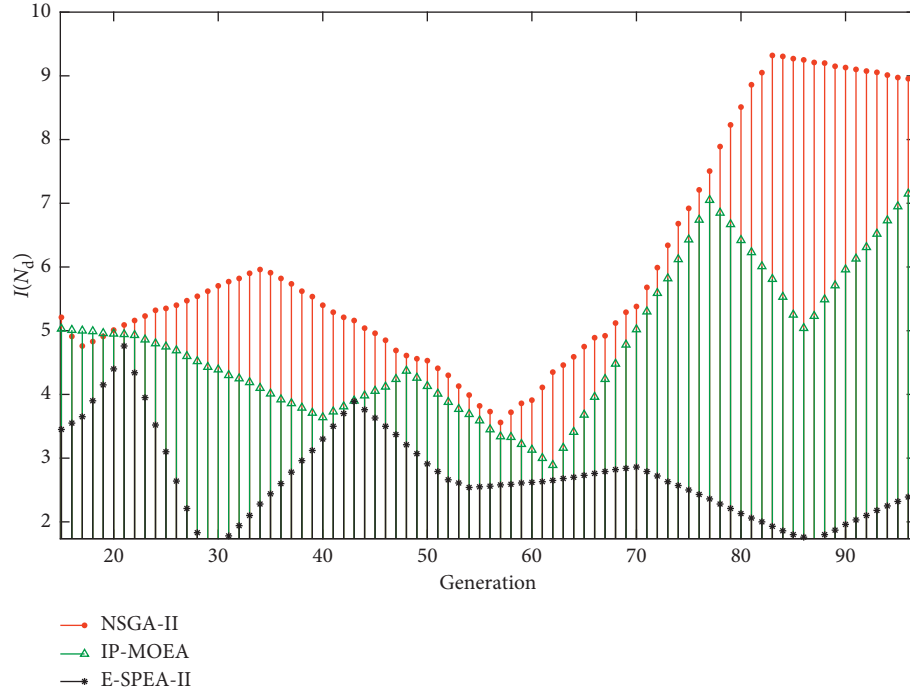


FIGURE 10: Imprecision (median).

$$I(N_d) := \sum_{f(x) \in N_d} \wedge \{x \mid \underline{f(x)} < y < \overline{f(x)}\}. \quad (54)$$

These three quantities are recorded when the ILCD problem is solved using three algorithms (NSGA-II, IP-MOEA, and E-SPEA-II). The hypervolume index $H(N_d)$ is shown in Figure 9: (a) With the increase of evolutionary generations, the performance of the Pareto optimal solution set obtained by the three methods is increasing. The Pareto front of the solution is getting closer to the real Pareto front synchronously. (b) For the same evolution generation, the $H(N_d)$ of the algorithm used in this paper is larger than the $H(N_d)$ of NSGA-II and IP-MOEA. The distribution degree $D(X)$ is shown in Table 11: the $D(X)$ of NSGA-II is 77.80% of the algorithm used in this paper. The $D(X)$ of IP-MOEA is 28.64% of the algorithm used in this paper. The imprecision index $I(N_d)$ is shown in Figure 10: (a) With the continuous change of the population, the $I(N_d)$ of the three algorithms is sometimes large and sometimes small, which shows that although the performance of the Pareto optimal solution sets of the three algorithms is increasing, the uncertainty of these solutions is very unstable. (b) For the same evolution generation, the $I(N_d)$ of the algorithm used in this paper is smaller than the one of IP-MOEA all the time and it is smaller than the one of NSGA-II most of the time.

In summary, the performance of the algorithm used in this paper is much better than the one of the two classic algorithms.

7. Conclusion

LCD is significant for enhancing the green quality at the beginning of life cycle for IMM. Nevertheless, the product

structure design and the product manufacturing process design are separated in the existing LCD method. It is thoughtless to consider the carbon emissions of one part. The ILCD method is proposed to solve this problem. After the carbon emissions model is constructed, an optimization method is used to find the optimal scheme of IMM.

There is still room for further research in IMM LCD: (1) The carbon emissions during the IMM maintenance and disassembly are not considered in this paper, which are parts of life cycle for IMM as well. (2) As an important component of injection industry, injection mold is of no use after the certain injection molding production is manufactured. It is effective to reuse the injection mold for reducing the carbon emissions.

Nomenclature

- C_B : Heat capacity of the material of extruder barrel, J/(kg·K)
- C_C : Heat capacity of the polymer, J/(kg·K)
- C_S : Heat capacity of the material of injection screw, J/(kg·K)
- C_W : Heat capacity of the heating roll, J/(kg·K)
- d_B : Inner diameter of the barrel, mm
- d_m : Embryo ring thickness of the polymer, mm
- E_R : Relative maximum of absolute error, %
- k_c : Coefficient of the cooling performance
- k_m : Thermal conductivity of the material, kW/(mm·K)
- L_{HB} : Length of the heating barrel, mm
- L_S : Length of the extruder barrel, mm
- m_B : Quality of the extruder barrel, kg
- m_S : Quality of the injection screw, kg
- m_{inj} : Injection mass, g

- N_a : Number of heating segments
 N_1 : Protruding length of nozzle, mm
 n_s : Screw-rated speed, r/min
 N_T : Nozzle type
 p : Plasticizing pressure, MPa
 ΔP : Pressure difference of the feed section of the screw, MPa
 p_{inj} : Injection pressure, MPa
 q_m : Displacement of the hydraulic motor, L/r
 R_c : Correlation coefficient, %
 r_{ld} : Length-to-diameter ratio of screw, mm
 t_B : Heating time of the extruder barrel, s
 t_s : Heating time of the injection screw, s
 v_{inj} : Injection rate, g/s
 V_C : Theoretical capacity, cm³
 ω_f : Polymer heat of fusion (zero for amorphous polymers), J/K kg
 ΔT_H : Temperature difference between the inner and outer surface of embryo ring thickness of the polymer, K
 ΔT_B : Temperature difference between the inner and outer surface of metering section of the extruder barrel, K
 ΔT_S : Temperature difference between the injection screw and the external environment, K
 τ_{h1} : Time-equivalent coefficient of the feed depth in rough machining, s/mm
 τ_{h2} : Time-equivalent coefficient of the feed depth in finish machining, s/mm
 τ_{HB1} : Time-equivalent coefficient of the length of the heating barrel in rough machining, s/mm
 τ_{HB2} : Time-equivalent coefficient of the length of the heating barrel in finish machining, s/mm
 $\tau_{\beta 1}$: Time-equivalent coefficient of the helix angle in finish machining, s/mm
 $\tau_{\beta 2}$: Time-equivalent coefficient of the helix angle in finish machining, s/mm
 μ_1 : Effective viscosity of the polymer in the screw groove, Pa·s
 μ_2 : Effective viscosity of the polymer in the gap, Pa·s

Data Availability

The data used to support the findings of this study are included within the article.

Conflicts of Interest

The authors declare that they have no conflicts of interest.

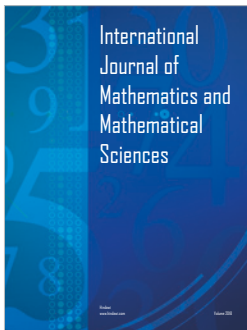
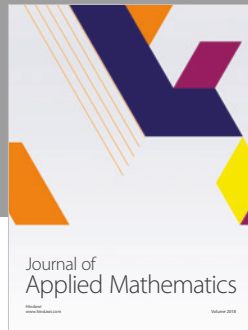
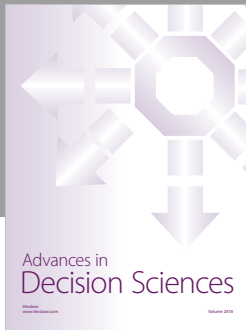
Acknowledgments

This work has been funded by the National Key R&D Program of China (2018YFB1700700), the National Natural Science Foundation of China (51875516), the Youth Funds of the State Key Laboratory of Fluid Power and Mechatronic Systems of Zhejiang University (SKLoFP_QN_1702), and the Collaborative Innovation Center of High-End Manufacturing Equipment.

References

- [1] X. T. Wang, *Injection Molding Technology and Injection Molding Machine*, Chemical Industry Press, Beijing, China, 2005.
- [2] National Bureau of Statistics of China, http://www.cnzbsl.com/News_View.asp?News_ID=619.
- [3] V. R. P. E. Dominick, V. R. P. D. Donald, and G. R. P. E. Marlene, *Injection Molding Handbook*, Springer US, New York, USA, 2000.
- [4] T.-S. Lan, K.-C. Chuang, and Y.-M. Chen, "Automated green innovation for computerized numerical-controlled machining design," *Advances in Mechanical Engineering*, vol. 10, no. 7, Article ID 168781401878977, 2018.
- [5] Q. Dai, Y. Li, Q. Xie, and L. Liang, "Allocating tradable emissions permits based on the proportional allocation concept to achieve a low-carbon economy," *Mathematical Problems in Engineering*, vol. 2014, Article ID 462705, 8 pages, 2014.
- [6] J.-S. Song and K.-M. Lee, "Development of a low-carbon product design system based on embedded GHG emissions," *Resources, Conservation and Recycling*, vol. 54, no. 9, pp. 547–556, 2010.
- [7] X. F. Zhang, S. Y. Zhang, Z. Y. Hu, G. Yu, C. H. Pei, and R. N. Sa, "Identification of connection units with high GHG emissions for low-carbon product structure design," *Journal of Cleaner Production*, vol. 27, pp. 118–125, 2012.
- [8] Q. Lu, G. H. Zhou, and Z. D. Xiao, "A selection methodology of key parts based on the characteristic of carbon emissions for low-carbon design," *The International Journal of Advanced Manufacturing Technology*, vol. 94, no. 9–12, pp. 3359–3373, 2018.
- [9] B. G. Chou, H. Z. Cai, G. Zhou, Y. J. Zhang, and J. Zhuang, "Design and motion simulation of the clamping mechanism of micro-structure injection molding machine," *Advanced Materials Research*, vol. 945–949, pp. 670–675, 2014.
- [10] R. Dubay, B. Pramujati, J. Han, and F. Strohmaier, "An investigation on the application of predictive control for controlling screw position and velocity on an injection molding machine," *Polymer Engineering & Science*, vol. 47, no. 4, pp. 390–399, 2007.
- [11] L. Shu, Y. Cai, M. Zhang, and Q. Wang, "CAE optimization and design of injection mould with inner parting structure for automobile front bumper," *Recent Patents on Materials Science*, vol. 9, no. 1, pp. 58–63, 2016.
- [12] A. Agazzi, V. Sobotka, R. Legoff, and Y. Jarny, "Optimal cooling design in injection moulding process—a new approach based on morphological surfaces," *Applied Thermal Engineering*, vol. 52, no. 1, pp. 170–178, 2013.
- [13] C. G. Li, C. L. Li, Y. Liu, and Y. Huang, "A new C-space method to automate the layout design of injection mould cooling system," *Computer-Aided Design*, vol. 44, no. 9, pp. 811–823, 2012.
- [14] X. C. Tan, F. Liu, H. J. Cao, and H. Zhang, "A decision-making framework model of cutting fluid selection for green manufacturing and the case study," *Journal Material Process Technology*, vol. 129, no. 1, pp. 467–470, 2002.
- [15] S. P. Sivapirakasam, J. Mathew, and M. Surianarayanan, "Multi-attribute decision making for green electrical discharge machining," *Expert System Application*, vol. 38, no. 7, pp. 8370–8374, 2011.
- [16] Z. Jiang and H. Zhang, "A vector projection method to evaluating machine tool alternatives for green manufacturing," in *Proceedings of the International Technology and*

- Innovation Conference 2006*, Hangzhou, China, November 2006.
- [17] H. S. Park and T. T. Nguyen, "Optimization of injection molding process for car fender in consideration of energy efficiency and product quality," *Journal of Computer Design Engineering*, vol. 1, no. 4, pp. 256–265, 2014.
- [18] J. Madan, M. Mani, J. H. Lee, and K. W. Lyons, "Energy performance evaluation and improvement of unit-manufacturing processes: injection molding case study," *Journal of Cleaner Production*, vol. 105, pp. 157–170, 2015.
- [19] E. Müller, R. Schillig, T. Stock, and M. Schmeiler, "Improvement of injection molding processes by using dual energy signatures," *Procedia CIRP*, vol. 17, pp. 704–709, 2014.
- [20] I. Meekers, P. Refalo, and A. Rochman, "Analysis of process parameters affecting energy consumption in plastic injection molding," *Procedia CIRP*, vol. 69, pp. 342–347, 2018.
- [21] J. B. Tranter, P. Refalo, and A. Rochman, "Towards sustainable injection molding of ABS plastic products," *Journal of Manufacturing Process*, vol. 29, pp. 399–406, 2017.
- [22] Z. J. Wang, Z. H. Zhan, Y. Lin et al., "Automatic niching differential evolution with contour prediction approach for multimodal optimization problems," *IEEE Transactions on Evolutionary Computation*, p. 1, 2019.
- [23] C. Liu, Q. Zhao, B. Yan, S. Elsayed, T. Ray, and R. Sarker, "Adaptive sorting-based evolutionary algorithm for many-objective optimization," *IEEE Transactions on Evolutionary Computation*, vol. 23, no. 2, pp. 247–257, 2018.
- [24] D. Chen, S. Singh, L. Gao, A. Garg, Z. Fan, and C. Wang, "A coupled and interactive influence of operational parameters for optimizing power output of cleaner energy production systems under uncertain conditions," *International Journal of Energy Research*, vol. 43, no. 3, pp. 1294–1302, 2019.
- [25] Z. L. Wang, S. Y. Zhang, and L. M. Qiu, "A new low-carbon design method based on multi-agent interactive reinforcement learning," *Proceedings of the Institution of Mechanical Engineers, Part C: Journal of Mechanical Engineering Science*, vol. 233, no. 2, pp. 539–553, 2019.
- [26] B. Li, J. Hong, and Z. Liu, "A novel topology optimization method of welded box-beam structures motivated by low-carbon manufacturing concerns," *Journal of Cleaner Production*, vol. 142, pp. 2792–2803, 2017.
- [27] Q. C. Liu, S. F. Liu, and L. Q. Kun, "Decomposition and decoupling analysis of energy-related carbon emissions from China manufacturing," *Mathematical Problems in Engineering*, vol. 2015, Article ID 268286, 9 pages, 2015.
- [28] A. Dietmair and A. Verl, "Energy consumption modeling and optimization for production machines," in *Proceedings of the IEEE International Conference on Sustainable Energy Technologies*, pp. 574–579, Seoul, South Korea, November 2008.
- [29] Y. Nakahara, M. Sasaki, and M. Gen, "On the linear programming problems with interval coefficients," *International Journal of Computer Industry Engineering*, vol. 23, no. 1–4, pp. 301–304, 1992.
- [30] G. Facchinetti, R. G. Ricci, and S. Muzzioli, "Note on ranking fuzzy triangular numbers," *International Journal of Intelligent System*, vol. 13, no. 7, pp. 613–622, 1998.
- [31] L. F. Sun, "Carbon emission hierarchical model of complex equipment for low-carbon design," *Computer Integrated Manufacturing System*, vol. 18, no. 11, pp. 2381–2390, 2012.
- [32] N. Cressie, "The origins of kriging," *Mathematical Geology*, vol. 22, no. 3, pp. 239–252, 1990.
- [33] J. P. C. Kleijnen, "Riging metamodeling in simulation: a review," *European Journal of Operational Research*, vol. 192, no. 3, pp. 707–716, 2009.
- [34] Z. Zhang, R. Tang, T. Peng, L. Tao, and S. Jia, "A method for minimizing the energy consumption of machining system: integration of process planning and scheduling," *Journal of Cleaner Production*, vol. 137, pp. 1647–1662, 2016.
- [35] J. Lv, R. Tang, and S. Jia, "Therblig-based energy supply modeling of computer numerical control machine tools," *Journal of Cleaner Production*, vol. 65, pp. 168–177, 2014.
- [36] Z. T. Yang, B. H. Wei, and J. P. Qu, "Application of accumulator to entire hydraulic injection molding machine and its energy-saving effect analysis," *Journal of Sichuan University*, vol. 42, no. 1, pp. 243–248, 2010.
- [37] PowerKnot—COPs, EERs, and SEERs: How Efficient Is Your Air Conditioning System?, <http://www.powerknot.com/how-efficient-is-your-air-conditioning-system.html>. 2014.
- [38] J. Mattis, P. Sheng, and W. Discipio, "A framework for analyzing energy efficient injection-molding die design," in *Proceedings of the IEEE International Symposium on Electronics and the Environment*, pp. 207–212, Orlando, FL, USA, May 1996.
- [39] E. Zitzler, M. Laumanns, and L. Thiele, "SPEA2: Improving the strength pareto evolutionary algorithm for multiobjective optimization," in *Proceedings of the EUROGEN Evolutionary Methods for Design, Optimization and Control with Applications to Industrial Problems*, Athens, Greece, September, 2001.
- [40] D. K. Saxena, T. Ray, K. Deb, and A. Tiwari, "Constrained many-objective optimization: a way forward," in *Proceedings of the IEEE Press Eleventh Conference on Congress on Evolutionary Computation*, pp. 545–552, Trondheim, Norway, May 2009.
- [41] G. Guo, H. Wang, D. Bell, Y. Bi, and K. Greer, "KNN model-based approach in classification," in *Lecture Notes Computer Science*, vol. 2888, pp. 986–996, Springer Science + Business Media, Berlin, Germany, 2003.
- [42] K. S. Yoon and C. Hwang, "Manufacturing plant location analysis by multiple attribute decision making: part II multi-plant strategy and plant relocation," *International Journal of Production Research*, vol. 23, no. 2, pp. 361–370, 1985.
- [43] L. L. Kong, *Research on CNC Machine Tool Energy Modeling and Analysis of Its Influential Parameters*, Dalian University Technology of China, Dalian, China, 2014.
- [44] Polaris Power News Network, Analysis of Power and New Energy Development Situation in 2017, <http://news.bjx.com.cn/html/20170112/803057.shtml>.
- [45] K. Deb, A. Pratap, and S. Agarwal, "A fast and elitist multi-objective genetic algorithm: nsga-II," *IEEE Transaction Evolutionary Computation*, vol. 6, no. 2, pp. 182–197, 2002.
- [46] P. Limbourg and D. E. S. Aponte, "An optimization algorithm for imprecise multi-objective problem functions," in *Proceedings of the 2005 IEEE Congress on IEEE Evolutionary Computation*, vol. 1, pp. 459–466, Edinburgh, Scotland, September 2005.



Hindawi

Submit your manuscripts at
www.hindawi.com

